

# Evidences of the supercritical disc funnel radiation in X-ray spectra of SS 433

A. Medvedev,<sup>1</sup> S. Fabrika<sup>2</sup>

<sup>1</sup> *Moscow State University, Russia, Moscow*

<sup>2</sup> *Special Astrophysical Observatory, Russia, Nizhij Arkhyz*

Accepted 2009 October 16. Received 2009 September 23; in original form 2009 June 03

## ABSTRACT

We have analysed the XMM-Newton spectra of SS 433 using a standard model of adiabatically and radiatively cooling X-ray jets. The multi-temperature thermal jet model reproduces well the strongest observed emission line fluxes. Fitting the He- and H-like iron line fluxes, we find that the visible blue jet base temperature is  $\approx 17$  keV, the jet kinetic luminosity  $L_k \sim 2 \cdot 10^{39}$  erg/s and the absorbing column density  $N_H \sim 1.5 \cdot 10^{22}$  cm<sup>-2</sup>. All these parameters are in line with the previous studies. The thermal model alone can not reproduce the continuum radiation in the XMM spectral range, the fluorescent iron line and some broad spectral features. Using the thermal jet-plus-reflection model, we find a notable contribution of ionized reflection to the spectrum in the energy range from  $\sim 3$  to 12 keV. The reflecting surface is highly ionized ( $\xi \sim 300$ ), the illuminating radiation photon index changes from the flat spectrum ( $\Gamma \approx 2$ ) in the 7–12 keV range to  $\Gamma \approx 1.6$  in the range of 4–7 keV, and to  $\Gamma \lesssim 1$  in the range of 2–4 keV. We conclude that the reflected spectrum is an evidence of the supercritical disc funnel, where the illuminating radiation comes from deeper funnel regions, to be further reflected in the outer visible funnel walls ( $r \gtrsim 2 \cdot 10^{11}$  cm). In the multiple scatterings in the funnel, the harder radiation  $> 7$  keV may survive absorption, but softer radiation is absorbed, making the illuminating spectrum curved. We have not found any evidences of reflection in the soft 0.8–2 keV energy range, instead, a soft excess is detected, that does not depend on the thermal jet model details. However the soft component spectrum is basically unknown. This soft component might prove to be the direct radiation of the visible funnel wall. It is represented here either as black body radiation with the temperature of  $\theta_{bb} \approx 0.1$  keV and luminosity of  $L_{bb} \sim 3 \cdot 10^{37}$  erg/s, or with a multicolour funnel (MCF) model. The soft spectral component has about the same parameters as those found in ULXs.

**Key words:** massive close binaries – stellar mass black holes: individual: SS 433 – X-ray spectra: supercritical accretion discs – ULXs.

## 1 INTRODUCTION

SS 433 is the only known persistent superaccretor in the Galaxy – a source of relativistic jets (Fabrika 2004, for review). This is a massive close binary, where the compact star is most probably a black hole (Gies, Huang, & McSwain 2002; Cherepashchuk et al. 2005; Hillwig & Gies 2008; Blundell, Bowler, & Schmidtobreick 2008). SS 433 intrinsic luminosity is estimated to be  $\sim 10^{40}$  erg/s, with its maximum located in non-observed UV region. In effect this is a very blue, but heavily absorbed object; its estimated temperature depends on the accretion disc orientation (Murdin, Clark, & Martin 1980; Cherepashchuk, Aslanov, & Kornilov 1982; Dolan et al. 1997), being  $\sim 50000 - 70000$  K when the disc is the most

open to the observer. It is important that almost all the observed radiation is formed in the supercritical accretion disc, and the donor star contributes less than 20% of the optical radiation. The system’s extreme luminosity suggests that the black hole’s mass is  $\sim 10 M_\odot$ . Such a big energy budget of the object is supported by a very well measured kinetic luminosity of the jets,  $\sim 10^{39}$  erg/s, both in direct X-ray and optical studies of the jets and in the studies of the jet-powered nebula W 50 (Fabrika 2004). At the same time we know that practically all the energy at the accretion onto a relativistic star is released in X-rays. This means that the observed radiation of SS 433 was thermalised in the strong wind coming from the supercritical disc.

The wind from a supercritical disc was first predicted by Shakura & Syunyaev (1973) and later

confirmed in radiation-hydrodynamic simulations (Eggum, Coroniti, & Katz 1988; Okuda et al. 2005; Ohsuga et al. 2005). These ideas led to a prediction that SS 433, being observed face-on appears as an extremely bright X-ray source, and we may expect an appearance of a new type of X-ray sources in galaxies (Katz 1987; Fabrika & Mescheryakov 2000, 2001) – the face-on SS 433 stars. It is quite possible that the new type of X-ray sources, ULXs (ultraluminous X-ray sources, Roberts (2007)) are SS 433-like objects observed nearly face-on. Their observed X-ray luminosities are  $10^{39} - 3 \cdot 10^{41}$  erg/s and they are certainly related to the massive star population. The disc orientation in SS 433 is about edge-on, the angle between the disc plane and the line of sight is  $10 \pm 20^\circ$ , due to the precessional variations. Therefore we have no chance to observe the funnel in the supercritical disc directly.

The supercritical disc radiation is not isotropic. If one takes into account the geometrical beaming in the disc funnel with the (half) opening angle  $\vartheta_f \sim 25^\circ - 30^\circ$  (Ohsuga et al. 2005) and that a supercritical disc surface radiation is local Eddington (Shakura & Syunyaev 1973), one finds (Fabrika et al. 2006), that the observed X-ray luminosity of  $\sim 10^{41}$  erg/s is expected for the face-on SS 433 star. The recent data show (Stobbart, Roberts, & Wilms 2006; Bergeha et al. 2008) that ULXs possess curvature and rather flat X-ray spectra, which are difficult to interpret with a single-component or any other simple model. The supercritical accretion discs are expected to have flat ( $\nu F_\nu \propto \nu^0$ ) X-ray spectrum (Poutanen et al. 2007), because the energy release  $Q(r)$  in the discs must be  $Q(r) \propto r^{-2}$  ( $T(r) \propto r^{-1/2}$ ) to make the disc thick due to the radiation pressure.

The X-ray luminosity of SS 433 is  $\sim 10^{36}$  erg/s (at a distance of 5.5 kpc (Blundell & Bowler 2004)), four orders of magnitude less than the bolometric luminosity. It is believed that all the X-rays come from the cooling X-ray jets. The jet may be easily accelerated by the radiation in the hydrodynamic funnel (e.g., Ohsuga et al. 2005) of the supercritical disc. The jet velocity value,  $v_j \approx 0.26c$ , and its unique stability, where the velocity does not depend on the activity state, indicate that the jet acceleration must be controlled by the line-locking mechanism (Shapiro, Milgrom, & Rees 1986; Fabrika 2004). The funnel has to be relatively transparent for the accelerating radiation, as it was confirmed in radiation-hydrodynamic simulations (e.g., Ohsuga et al. 2005).

These reasonings, however, bear a problem, why do not we observe any funnel radiation, missing four orders of magnitude in the X-rays? Even a small amount of gas in the most outer part of the funnel, where we observe the X-ray jet base, may reflect and scatter some part of the direct  $\sim 10^{40}$  erg/s of the funnel radiation. The structure of the funnel and the jet acceleration/collimation region is unknown. Apparently, the direct funnel radiation is entirely blocked for the observer. The 'standard' jet model (Brinkmann et al. 1988; Kotani et al. 1996; Marshall, Canizares, & Schulz 2002; Filippova et al. 2006) suggests that all the observed X-ray radiation of SS 433 is formed in the cooling X-ray jets. However, an analysis of the latest XMM observations (Brinkmann, Kotani, & Kawai 2005) led the authors to a conclusion that the 'standard' jet model can not produce the observed X-ray continuum.

In the 'standard' jet model there are two conical anti-

parallel jets, considered identical. The jet's gas is optically thin, being in collisional ionization equilibrium and cooling adiabatically (or adiabatically plus radiatively). The jets are observed beginning from the jet base  $r_0$  (the distance between the base of the visible jet and the black hole, different for the red and blue jets), which depends on the precessional phase and on the eclipses by the donor star. The gas temperature at the jet base  $T_0(r_0)$  is estimated from observations. Precessional and orbital variability of SS 433 is well-known (Fabrika 2004), the jets (and both the accretion disc, and the accretion disc wind) precess with a 164-day period and an amplitude of  $\pm 20^\circ$ . At the precessional phase  $\psi \approx 0$  the disc is the most open to the observer, the angle between the jets and line of sight is  $\sim 60^\circ$  (we refer here to the approximate values because there are nutation-like and sporadic variabilities, both of about  $3 - 5^\circ$ ). The accretion disc rim (or the opaque part of the wind) is thick  $h/r \sim 1$  (Filippova et al. 2006). Comparing the amplitudes of the precessional and orbital variabilities in different X-ray bands, Cherepashchuk et al. (2005) found that both the donor star and the outer disc rim have about the same size. Therefore, one may expect the same radius for the approaching jet base  $r_0 \sim 10^{12}$  cm.

In X-ray observations with ASCA and Chandra (Kotani et al. 1996; Marshall, Canizares, & Schulz 2002), dozens of X-ray emission lines formed both in blue and red jets were resolved. The lines are variable both in positions (in accordance with the jet kinematic model) and in intensities, the strongest are He- and H-like Fe XXV  $K\alpha$  and Fe XXVII  $L\alpha$  iron lines. This allowed the 'iron line diagnostics' of the gas temperature at the jet bases by measuring the line ratio Fe XXV/Fe XXVI. The temperature at the base of the jet was estimated as  $\theta_0 = kT_0 = 10 \div 20$  keV (Kotani et al. 1996; Marshall, Canizares, & Schulz 2002; Namiki et al. 2003). In the latest XMM-Newton observations Brinkmann, Kotani, & Kawai (2005) estimate the temperature of about  $\theta_0 \sim 17 \pm 2$  keV, with the main uncertainty coming from the form of the underlying continuum. Fitting the continuum with a thermal bremsstrahlung model (GINGA data, Brinkmann et al. 1991) gives a notably bigger value,  $\theta_0 \gtrsim 30$  keV. The jet base temperature determined both in the line diagnostics and in the continuum fits, drops notably in eclipses, what confirms the cooling jet model. Analysing the numerous ASCA data, Kotani et al. (1996) found that the farther part of the receding jet is weakened (probably absorbed in the external gas located in the disc plane) and Nickel is highly overabundant ( $\sim 10$  times) in the jets. The last finding has been confirmed in the XMM observations (Brinkmann, Kotani, & Kawai 2005). Note that some discrepancies may exist as the system SS 433 is highly variable and its appearance depends strongly on the precessional phase.

Brinkmann, Kotani, & Kawai (2005) found that the XMM SS 433 spectrum can not be fitted with any simple continuum law. The numerous lines point at the thermal model, but a strong continuum curvature indicates the Comptonization. The best formal model of the additional continuum component is a broken power law with a break at  $\sim 7.1$  keV, where the low energy PL rises with energy ( $\Gamma \sim -1$ ), the high energy part is rather steep ( $\Gamma \sim 4$ ), however, the parameters are not usually well determined in the fits. The overall continuum is too hard to be bremsstrahlung,

the electron-electron bremsstrahlung can not fit it even for the temperatures of 40 keV. A highly absorbed additional thermal component gives a too strong  $\sim 7$  keV edge. Brinkmann, Kotani, & Kawai (2005) discuss a model with a single, very broad  $\sim 7$  keV line, which may be formed in the innermost hot jet (otherwise hidden) and Compton down-scattered by colder material. These uncertainties in continuum make problems for the iron-line diagnostics of the jet base temperature.

Practically in all the studies of SS 433 X-ray spectra the jet mass loss  $\dot{M}_j$  and the jet kinetic luminosity  $L_k = \dot{M}_j v_j^2 / 2$  were determined. To estimate  $L_k$  one needs to adopt the jet (half) opening angle  $\vartheta_j$ . The mass loss rate derived from the X-ray line intensities depends strongly on the opening angle adopted, i. e. gas density at the jet base, because the emission measure is  $\propto n^2$ . The kinetic luminosity values derived from X-ray spectra were quite diverse, up to  $10^{42}$  erg/s. However, in two latest studies, one from the Chandra data (Marshall, Canizares, & Schulz 2002) and the other from the XMM data (Brinkmann, Kotani, & Kawai 2005), the values are  $\sim 3 \cdot 10^{38}$  and  $\sim 5 \cdot 10^{39}$  erg/s respectively. They are even closer to one another, matching different distances to SS 433 adopted by these authors. Panferov & Fabrika (1997) found  $L_k \sim 10^{39}$  erg/s from the jet Balmer line intensities in optical spectra. The mass loss rate in the jets was estimated (Zealey, Dopita, & Malin 1980; Fabrika & Borisov 1987; Dubner et al. 1998) on the base of W 50 nebula powered by the jets with approximately the same result,  $L_k \sim 10^{39}$  erg/s. Thus the jet kinetic luminosity was measured with relatively good accuracy.

The jet opening angle was directly measured in the studies of X-ray and optical line widths (Fabrika 2004). Marshall, Canizares, & Schulz (2002) found  $\vartheta_j = 0.61 \pm 0.03^\circ$  from the Chandra spectra. They assumed that the density is uniform through the jet cone's cross section and  $\vartheta_j$  is the jet's cross sectional radius. Borisov & Fabrika (1987) found  $\vartheta_j = 0.82 \pm 0.14^\circ$  from optical spectra, assuming that the emitting gas density is Gaussian-distributed in the cone's cross section. We give here the values of  $\vartheta_j$  recalculated, using the Marshall, Canizares, & Schulz (2002) definition. Such a coincidence in the X-ray and optical jet opening angles makes the jets pure ballistic from X-ray ( $\sim 10^{12}$  cm) to optical ( $\sim 10^{15}$  cm) regions. In optical spectra the jet opening angle has been estimated from H $\alpha$  line profiles during 8-day long observations, the nutation broadening has been taken into account and possible jet sporadic activity was diminished. In other Chandra observations (Namiki et al. 2003; Lopez et al. 2006) the opening angle has been found twice as big and it was greater in the higher temperature (Fe), than in the lower temperature (Si) parts of the jets. Regarding comparatively short time scales of the X-ray observations and probable line broadening due to electron scattering (Namiki et al. 2003) in the hottest parts of the jet, we may adopt  $\vartheta_j \approx 0.7^\circ$  as a good estimate of the jet opening angle.

In this paper we analyse X-ray spectra of SS 433 using XMM data and the 'standard' jet model. We do not try to determine the jet kinetic luminosity, because the X-ray continuum is complex and can not be explained in the 'standard' jet model (Brinkmann, Kotani, & Kawai 2005). Instead we adopt these two main parameters –  $L_k = 10^{39}$  erg/s ( $\dot{M}_j = 3.3 \cdot 10^{19}$  g/s) and  $2\vartheta_j = 1.5^\circ$ , as well established and

known. We find that the line fluxes can be well matched with the 'standard' jet model and study the additional components of the X-ray spectrum of SS 433.

## 2 OBSERVATIONS AND DATA REDUCTION

We used a public archive of the XMM-Newton Observatory.<sup>1</sup> There are 8 observations of SS 433 in the archive, where the target was in the detector's centre. They were carried out in April 2003 (4 observations at the precessional phase  $\psi \approx 0.8$ ), October 2003 (2 observations at  $\psi \approx 0$ ), and two single observations in March 2004 and April 2004. In this paper we concentrate on the study of X-ray jets and the thick accretion disc (its wind). Then we have selected only those observations, where disc was not eclipsed by the donor and was the most open to the observer. This is the observation taken on 19 October 2003 in orbit 707 ( $\psi = 0.04$ ) in the orbital phase  $\varphi = 0.28$  (for orbital and precessional phases see Fabrika (2004)). For comparison purposes we selected the observation from 6 April 2003 in orbit 609, taken at the intermediate inclination ( $\psi \approx 0.84$ ) of the disc and at about the same orbital phase  $\varphi = 0.34$ . The last observation is relatively short, hence we added the following observation taken in the same accretion disc precessional position, in orbit 610 ( $\varphi = 0.49$ ) for a control check.

These data allow us to study the jets and the disc wind at two different orientations of the disc/jets and at about the same orbital phase. With such a strong mass transfer in the system, the jet and the accretion disc funnel visibility behind the wind photosphere (the outer disc rim) may be dependent on the orbital phase.

We use the EPIC PN observations to get the highest signal-to-noise data. During all the observations the EPIC PN camera was operated in the Small Window mode with a medium filter. The PN data were reprocessed using the XMMAS version 6.1. The actual Life Time of the detector after a correction for Good Time Intervals was 11.4 ksec in orbit 707, 4.4 ksec in orbit 609 and 5.6 ksec in orbit 610.

## 3 JET MODEL

To model the jet spectrum we use the standard approach which was used by many authors to analyse the X-ray spectra of SS 433 (Kotani et al. 1996; Brinkmann et al. 1991; Brinkmann, Kotani, & Kawai 2005; Filippova et al. 2006). This standard multi-temperature model describes well both the jet line spectrum and its variability. The jet gas moves in ballistic trajectories with a velocity  $v = 0.26c$ . In such a case the gas concentration can be written as follows:

$$n(r) = n_0 \left( \frac{r}{r_0} \right)^{-2}, \quad \text{where} \quad n_0 = \frac{1}{\Omega_j} \frac{\dot{M}_j}{\mu m_p v_j r_0^2}. \quad (1)$$

Here  $r_0$  is the visible jet base (the distance between the base and the black hole),  $\Omega_j = 2\pi(1 - \cos \theta_j)$  is the solid opening angle of the jet,  $\dot{M}_j$  – the mass loss rate in the jet,  $m_p$  – the mass of a proton,  $\mu$  – molecular weight. The gas temperature

<sup>1</sup> [http://xmm.vilspa.esa.es/external/xmm\\_data\\_acc/xsa/](http://xmm.vilspa.esa.es/external/xmm_data_acc/xsa/)

$\theta = kT$  along the jet accounting for adiabatic and radiation cooling is determined by the equation:

$$\frac{3}{2} \frac{d\theta}{\theta} - \frac{dn}{n} \left( 1 + \frac{r\tilde{\epsilon}}{2v_j\theta} \right) = 0, \quad (2)$$

where  $\tilde{\epsilon}$  stands for specific energy losses by radiation per one particle. Introducing new variables  $\tau = \theta/\theta_0$ ,  $x = r/r_0$ ,  $\tilde{\epsilon} = \mu n J$  one may write the equation (2) in a dimensionless form:

$$\frac{d\tau}{dx} = -\frac{4}{3} \frac{\tau}{x} - \alpha \frac{J(\tau; \theta_0)}{x^2}, \quad (3)$$

where  $\alpha$  is a coefficient depending on physical parameters of the jet  $\dot{M}_j$  and  $r_0$ :

$$\alpha = \frac{\mu}{\Omega_j m_p v_j^2} \frac{\dot{M}_j}{r_0 \theta_0}. \quad (4)$$

The introduced value  $J(\theta)$  is the total emissivity of the plasma, and radiation losses integrated over all energies,

$$J(\theta) = \int J_\epsilon(\theta) d\epsilon. \quad (5)$$

The value  $J(\theta)$  is tabulated in the model of hot, optically thin plasma APEC/APED, which uses the atomic database ATOMDB v1.3.1 (Smith et al. 2001a, Smith & Brickhouse 2000, Smith et al. 2001b). ATOMDB provides an improved spectral modelling capability through additional emission lines, accurate wavelengths for strong X-ray transitions, and new density-dependent calculations (for more details see <http://cxc.harvard.edu/atomdb/>). Relativistic boosting is taken into account in this model. The model provides a possibility of separate analysis of both line and continuum emissivities.

To calculate the multi-temperature jet spectrum we divide the jet in 20 equal parts in the section  $r_0 - 4r_0$ , the gas temperature at  $\sim 4r_0$  drops below 100 eV, where the thermal instabilities begin to operate (Kotani et al. 1996). One needs to consider many (at least 20) mono-temperature parts of the jet, because the radiative cooling begins to dominate the adiabatic cooling at temperatures below  $\sim 2$  keV and has a strong peak at  $\sim 0.6$  keV. The total spectrum of the jet is calculated using the formula:

$$F_\epsilon = \sum_i N_i J_\epsilon(\theta_i^*), \quad (6)$$

where  $J_\epsilon$  is the plasma emissivity and  $N_i$  is the spectrum normalisation of  $i$ -th part of the jet:

$$N_i = \frac{1}{4\pi D^2} \int_{V_i} n_e n_H dV, \quad (7)$$

where  $D$  is a distance to SS 433 (5.5 kpc, Blundell & Bowler 2004). The integration is carried out over the jet portion volumes  $V_j$ . The average gas temperature of the  $i$ -th part of the jet  $\theta_i^*$  is estimated as follows:

$$\theta_i^* = \frac{\int_{r_i} \theta(r) J(r) \frac{dr}{r^2}}{\int_{r_i} J(r) \frac{dr}{r^2}}. \quad (8)$$

The main parameters which define the physical state of the jet are gas density and temperature  $\theta_0(r_0)$  at the visible jet base. The density depends on the mass loss rate  $\dot{M}_j$  and the jet (half) opening angle  $\vartheta_j$ . As we discussed in the

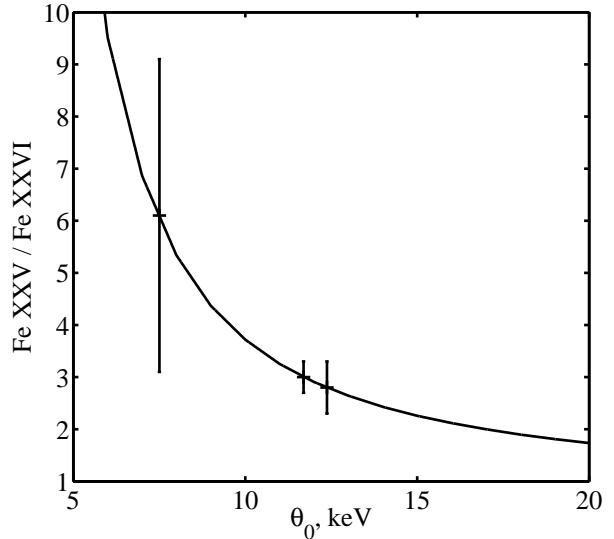


**Figure 1.** Measured ratio of the blue jet FeXXV and FeXXVI line fluxes (Table 1), derived with the simple local continuum fit, and the model ratio as depending on the gas temperature at the jet base. The highest temperature,  $\theta_0 \sim 12$  keV, is obtained in orbit 707 ( $\psi \approx 0.0$ ), a slightly lower temperature in orbit 610 ( $\psi \approx 0.8$ ); in orbit 609 we find the temperature  $\theta_0 \sim 8$  keV with notably bigger uncertainty.

Introduction, the last two parameters were relatively well measured in SS 433 in previous studies not only in X-ray range. The opening angle was particularly very well measured in optical studies. To make our analysis more certain we do not try to determine the jet kinetic luminosity (the mass loss rate) from the XMM spectra, the more so, that one has serious problems with an interpretation of continuum at  $\sim 7$  keV (Brinkmann, Kotani, & Kawai 2005). Therefore, we adopt the parameters  $L_{kin} = 10^{39}$  erg/s and  $2\vartheta_j = 1.5^\circ$  as already known.

From all previous X-ray studies we may expect the gas temperature at the base is in the range of  $\theta_0(r_0) = 8-20$  keV (see Introduction), and the visible jet base  $r_0 \sim 10^{12}$  cm. The last estimate is quite substantial, it was argued above, that both the donor star and the outer disc rim have about the same size (Cherepashchuk et al. 2005; Filippova et al. 2006). The partial eclipses of the X-ray jets by the donor observed in SS 433 prove the estimate of the X-ray jet base  $r_0$ .

In the thermal jet model we adopt the solar abundance of elements, however, Nickel is 10 times overabundant (Brinkmann, Kotani, & Kawai 2005). Section 5 discusses this in detail.

#### 4 JET PARAMETERS IN IRON LINE DIAGNOSTICS

In this section we estimate the jet parameters  $\theta_0$  and  $r_0$  using the fluxes and the flux ratio of the iron lines FeXXV  $K_\alpha$  and FeXXVI  $L\gamma_\alpha$  (Kotani et al. 1996; Brinkmann, Kotani, & Kawai 2005) and adopting a simple local PL continuum. These FeXXV and FeXXVI lines formed in the approaching jet are the strongest and well

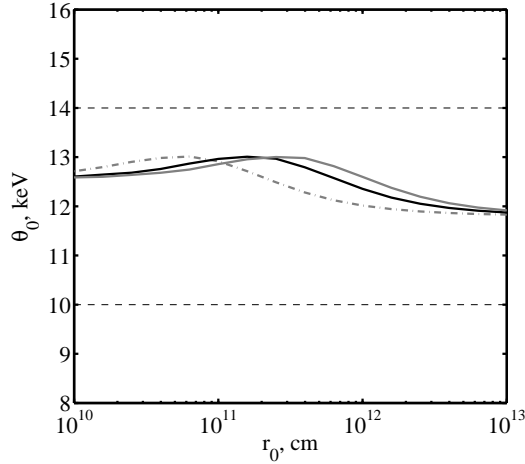


**Figure 2.** Dependence of the derived gas temperature at the jet base on the variations of the visible base position  $r_0$  (in the simple local continuum model) and mass loss rate  $\dot{M}_j$  for orbit 707 observation ( $\psi = 0$ ). The solid curve is for  $\dot{M}_j = 3.3 \times 10^{19}$  g/s ( $L_{kin} = 10^{39}$  erg/s), the dashed grey curve is for  $1.5 \times 10^{19}$ , the solid grey curve is for  $5 \times 10^{19}$  g/s. Two horizontal dashed lines mark the temperature limits (Table 1).

resolved in the XMM spectra. The resulting line fluxes depend on the underlying continuum model. Therefore we use the simplest continuum to analyse here how stable are the derived parameters depending on  $\dot{M}_j$  and on the errors of the measured line fluxes. We do not examine here different continuum models, because Brinkmann, Kotani, & Kawai (2005) have studied these XMM spectra using many versions of continuum and concluded that “the high sensitivity and wide bandpass of the XMM-Newton instruments rule out any of the simple continuum models used previously”. Instead in the section below we find clear evidences for a certain additional continuum component (reflection), study the whole spectrum with these two models, thermal jet and reflection, and correct the values of  $\theta_0$  and  $r_0$ .

In our model the iron line flux (as it follows from (6, 7)) may be written as:

$$F_l \propto J_l(\theta_0) \frac{\dot{M}_j^2}{\Omega_j r_0} \varphi(r_0, \dot{M}_j). \quad (9)$$

Here  $\varphi(r_0, \dot{M}_j)$  is a function depending on the gas cooling details and it does not strongly depend on  $r_0$  and  $\dot{M}_j$ . At the same time the line ratio Fe XXV/Fe XXVI depends on the gas temperature at the base  $\theta_0$  and its derivative  $d\theta/dr$ , which is determined by (3). Modelling of the iron line fluxes gives us information on the temperature and visible jet base  $r_0$ .

To determine the line fluxes in the observed spectra we model the continuum with power law, and the lines as Gaussian blueshifted to  $z = -0.105$  and  $z = -0.095$  for precessional phases  $\psi = 0$  and  $\psi = 0.8$  respectively. These blue shifts were found in our fits, and they are in approximative agreement with those expected from the precessional ephemeris. For better fits of these two lines with the continuum we discarded the spectral parts below  $< 7$  keV and  $8.0 - 9.5$  keV, where there is a complex of emission lines Ni XXVII, Ni XXVIII, Fe XXVII $\beta$  and Fe XXV K $\beta$ . This

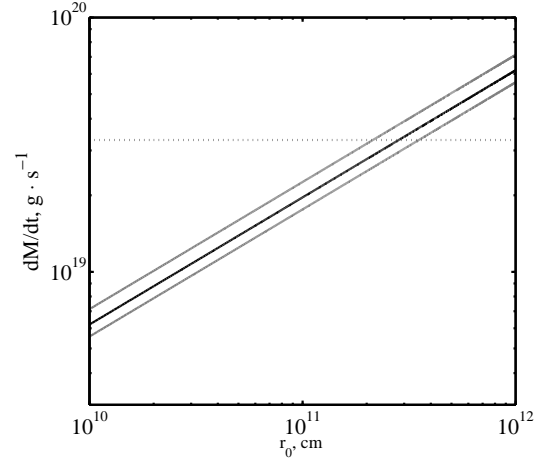


**Figure 3.** Determination of the blue jet visible base  $r_0$  from the Fe XXV line flux and the temperature derived (Table 1) for the observation in the precessional phase  $\psi = 0$ . To show confidence levels for  $r_0$  (two solid grey lines) we used triple errors of the line flux. Horizontal dashed line corresponds to the mass loss rate  $\dot{M}_j = 3.3 \times 10^{19}$  g/s ( $L_{kin} = 10^{39}$  erg/s).

spectral interval also includes a broad absorption feature (an absorption edge), which was reported by Kubota et al. (2007). In this simplest continuum model the line fluxes are well determined. Table 1 presents the fluxes of these two blueshifted lines and their ratios along with errors.

In Fig. 1 we show the observed flux ratios Fe XXV/Fe XXVI along with the model ratio depending on the gas temperature at the jet base. We check how stable is the temperature derived relating to the variations of  $\dot{M}_j$  and  $r_0$ . Fig. 2 shows the temperature as depending on  $r_0$  at different mass loss rates  $\dot{M}_j$  for the observation taken in the precessional phase  $\psi = 0$ . These two parameters do not change the base temperature notably. We find the same for the observations in the precessional phase  $\psi = 0.8$ . One may expect this result because the line flux (9) depends on  $\dot{M}_j$  and  $r_0$  in the same manner for both lines. Fig. 2 shows that to keep the same temperature at the visible jet base  $\theta_0(r_0)$  (the same iron line ratio), with bigger  $\dot{M}_j$  we have bigger  $r_0$  to have about the same gas density  $n_0(r_0)$ . The function  $\varphi(r_0, \dot{M}_j)$  depends on the gas density, which is  $n \propto \dot{M}_j/r_0^2$ .

There is also some interplay between the estimates of  $\theta_0(r_0)$  and  $r_0$  when we fix the mass loss rate in the jets. The emissivity of the Fe XXV line peaks at  $\theta \sim 5 - 6$  keV, and the total line flux is  $\propto n^2$ . When one finds  $\theta_0$  from the Fe XXV/Fe XXVI line ratio and determines the jet base  $r_0$  from the Fe XXV line flux, one obtains the gas density at the base  $n_0(r_0)$ . The higher the temperature  $\theta_0$  derived with regard to the 5–6 keV value, the lower the gas density in the emissivity peak jet region, the less  $r_0$  we obtain to match the observed line flux. This effect is seen in Fig. 2, and it is not strong.

Thus, we may find the temperature at the visible jet radius  $\theta_0(r_0)$  from the Fe XXV/Fe XXVI flux ratios, and then we may find the base ( $r_0$ ) from the observed flux of the blue shifted Fe XXV line and the derived temperature. The

**Table 1.** Observed fluxes and derived blue jet preliminary parameters in the simplest continuum model. The columns present precessional  $\psi$  and orbital  $\varphi$  phases of the observations, line fluxes in units  $10^{-4}$  ph/s cm<sup>2</sup>, the flux ratios  $\mathcal{R}$ , the temperature at the jet visible base  $\theta_0$  and the base  $r_0$ .

$\psi$	$\varphi$	F(Fe XXV)	F(Fe XXVI)	$\mathcal{R}$	$\theta_0$ , keV	$r_0$ , $10^{11}$ cm
0.04	0.28	$5.5 \pm 0.4$	$1.95 \pm 0.3$	$2.8 \pm 0.5$	$12 \pm 2$	$2.8 \pm 0.2$
0.84	0.34	$4.9 \pm 0.7$	$0.8 \pm 0.4$	$6.1 \pm 3$	$8 \pm 1$	$2.6 \pm 0.3$
0.84	0.49	$5.9 \pm 0.2$	$2.0 \pm 0.2$	$3.0 \pm 0.3$	$12 \pm 1$	$2.6 \pm 0.1$

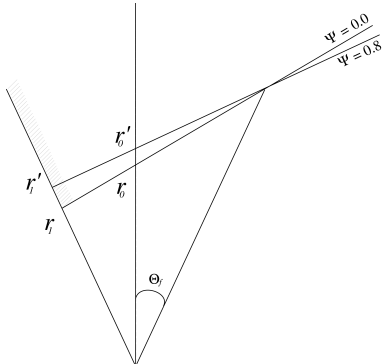


**Figure 4.** A sketch of the funnel and the blue jet visibility at two precessional phases considered.  $r_0$  ( $r'_0$ ) is the distance between the base of the visible jet and the top of the cone (the bottom of the funnel).  $r_1$  ( $r'_1$ ) is the distance between the base of the visible funnel wall and the top of the cone.

values of  $\theta_0(r_0)$  and  $r_0$  found with the simple continuum model are presented in Table 1.

Fig. 3 shows how the base  $r_0$  is determined from the FeXXV line flux. We used here the triple errors (Table 1) of the He-like blue jet line flux. The blue jet visible base we found is  $r_0 \sim 3 \cdot 10^{11}$  cm. The equation (9) provides us with useful and obvious scaling formula,  $r_0 \propto M_j^2 / \Omega_j$ , and Fig. 3 confirms the scaling. With different jet parameters satisfying this scaling and with about the same gas temperature at the visible jet base, we obtain about the same thermal jet spectra.

Fig. 4 shows a sketch of the jet and the supercritical accretion wind (funnel) geometry at two precessional phases which we consider,  $\psi \approx 0$  (orbit 707) and  $\psi \approx 0.8$  (orbits 609, 610). They are marked in the figure as  $r_0$  and  $r'_0$  respectively. We adopted the funnel opening angle  $\vartheta_f = 25^\circ$  (Ohsuga et al. 2005) in the figure. Our estimates of  $r_0$  and  $r'_0$  are the same within the errors (Table 1), however the result depends on the fluxes of the Fe XXV line, i. e. on the natural variability of SS 433 jet activity. In the second observation at the  $\psi \approx 0.8$  the iron line is brighter.

The estimates of  $\theta_0(r_0)$  and  $r_0$  obtained in this section were derived using the simplest continuum model. In this model we discarded the spectral part below  $< 7$  keV and the region of  $8.0 - 9.5$  keV, which includes a broad absorption edge (Kubota et al. 2007). This absorption feature may distort the Fe XXV / Fe XXVI line ratio making it higher, as a part of the Fe XXVI line profile may be inside of the broad edge. The edge profile is not established yet (Kubota et al. 2007), and we can not rule out that real temperature  $\theta_0(r_0)$  is somewhere higher than the one we derived here. Our estimate of  $r_0$  is not affected by the absorption edge, because

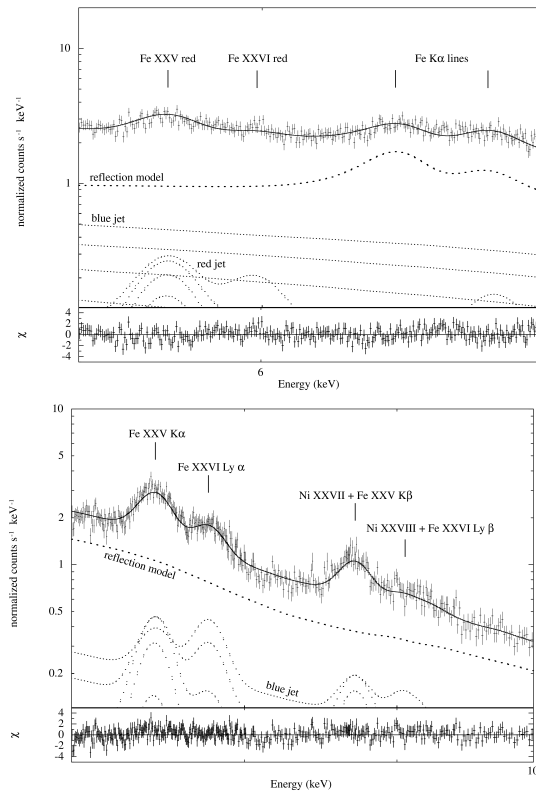


**Figure 5.** Observed spectrum of SS 433 (orbit 707,  $\psi \sim 0$ ) with the thermal jet model components and the additional reflection model in two spectral regions 5.0–7.0 keV (top) and 7.0–10.0 keV (bottom). The total model spectrum is shown with solid line. The reflection model explains well the fluorescence iron line at 6.4 keV, the recombination iron K $\alpha$  line of Fe XXV at 6.7 keV (top) and the iron absorption edge (Kubota et al. 2007) at  $\sim 8 - 9$  keV.

it is based on the Fe XXV line. We use these estimates of  $\theta_0(r_0)$  and  $r_0$  (Table 1) as a first approximation. Below we find more accurate values of these parameters using a more complex model of the continuum, which describes the whole spectrum of SS 433.

## 5 ADDITIONAL COMPONENTS IN SS 433 SPECTRA. REFLECTION MODEL

As it was noted in the Introduction, there is a problem of four orders of magnitude, missing in X-ray luminosity of SS 433. One may expect to find the original luminosity of the object  $L_x \sim 10^{40}$  erg/s, instead, we observe  $L_x \sim 10^{36}$  erg/s. This may mean that direct radiation is blocked inside the hydrodynamical funnel, where the jets are accelerated and

collimated (Fabrika 2004). Taking into account such an extreme original luminosity we may expect to observe a reflection of a part of the radiation at the outer funnel walls (the wind). In Fig. 4 we show the probable reflecting area on the wall at  $r > r_1$ .

There are strong observational indications that point to an existence of a reflection component in the X-ray spectrum of SS 433. Firstly, the presence of a strong fluorescent line of quasi-neutral iron (6.4 keV), which can be a result of the reflection. Secondly, in the spectral region  $\sim 8 - 9$  keV there is a broad absorption feature (a trough), detected by Kubota et al. (2007). The trough may be an iron absorption edge arising in reflection, its position corresponds not to the neutral plasma, but the some intermediate stages of iron ionization (Kubota et al. 2007). This leads to an assumption that the reflecting matter is partly ionized. That is why we decide to fit the observed spectrum of SS 433 with the multi-temperature jet model plus reflection in the partly ionized material.

For the reflection component we use the REFLION<sup>1</sup> model of X-ray ionized reflection (Ross, Fabian, & Young 1999; Ross & Fabian 2005). The illuminating radiation is assumed to have a cut-off power-law spectrum  $F_E = AE^{-\Gamma+1} \exp(-E/E_c)$ , where the cut-off energy is fixed at  $E_c = 300$  keV. It is assumed that the surface is irradiated with the X-rays so intense that its ionization state is determined by the ionization parameter,

$$\xi = \frac{4\pi F_{tot}}{n}, \quad (10)$$

where  $F_{tot} = \int F_E dE$  – the total illuminating flux,  $n$  – the surface gas density. The amplitude  $A$  in the total illuminating flux is chosen to provide a desired value of the ionization parameter  $\xi$ . In the model the irradiated gas is Compton thick and has a constant density. The illuminating radiation flux has a power-law spectrum in the model, and the photon index  $\Gamma$  is a model parameter.

Fig. 5 shows the observed spectrum of SS 433 with the thermal jet model and additional reflection model. It presents two regions 5.0–7.0 keV and 7.0–10.0 keV fitted with the same model parameters. Both the reflection emission feature at 6.4 keV and the iron absorption edge at  $\sim 8 - 9$  keV are reproduced well in the reflection model. Fig. 5 discovers one more evidence of the reflection in SS 433 spectrum, it is an emission feature of iron FeXXV K $\alpha$  at 6.7 keV at zero velocity. The REFLION model (Ross & Fabian 2005) considers the K $\alpha$  recombination lines of FeXXV–XXVI (near 6.7 and 7.0 keV) and the fluorescence lines of FeVI–XVI (near 6.4 keV). The fluorescence features never been explained before in SS 433 spectrum, this convinces us to use the reflection model as an additional (to the thermal jet) component. In the reflection model fit we estimate the ionization parameter at the reflecting surface of  $\xi \sim 300$  and the illuminating radiation spectral index of  $\Gamma \sim 2$ . The very good continuum fit allows us to estimate more accurately the iron line fluxes in the blue jet and respectively the visible jet base temperature, it is  $\theta_0(r_0) \sim 17$  keV. Below in this section we study these parameters in more details using the whole spectrum.

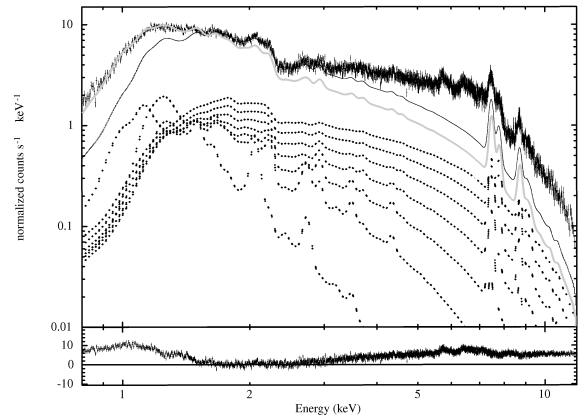


**Figure 6.** Observed spectrum of SS 433 (orbit 707,  $\psi \sim 0$ ) with two thermal jet models. The first model ( $\theta_0(r_0) = 17$  keV,  $N_H = 1.5 \times 10^{22} \text{ cm}^{-2}$ ) is shown with solid thin line, individual parts of the multi-temperature jet are shown with dashed lines together with the model’s residuals in bottom. The model produces well the blue jet lines in the region 7–9 keV. The second model ( $\theta_0(r_0) = 14$  keV,  $N_H = 1.0 \times 10^{22} \text{ cm}^{-2}$ ) is shown with grey thick line, this model is intended to fit the lower energy range, however it fails to produce observed line fluxes of the blue jet. The strong excess of the observed continuum radiation in the region  $> 2.5$  keV may be fitted well with the reflection additional component (section 5).

The harder part of the spectrum  $> 5$  keV is not sensitive to the absorption value  $N_H$ , from the other hand, the reflection component we found weakens notably in softer energies,  $< 4$  keV. That is why to study the absorption value  $N_H$ , in a next step we analyse the whole spectrum of SS 433 with the thermal jet component only.

In Fig. 6 we show the observed spectrum of SS 433 along with the thermal blue jet models. We only used in our figure the blue jet, because adding the red jet can not in effect solve the continuum problems both at higher energy and even at lower energies (Brinkmann, Kotani, & Kawai 2005). Kotani et al. (1996) have found that the receding red jet is not visible in low energy ranges (in the ranges  $< 4$  keV) in the precessional phases  $\psi \sim 0$ , when the accretion disc is the most open to the observer. They interpreted this fact via an existence of absorbing gas in the precessing plane perpendicular to the jets (the accretion disc plane), which only blocks the outer cooler parts of the red jet. The hotter parts of the red jet located closer to the central machine, are visible, the extended material does not obscure them. The extended precessing disc-like outflow in SS 433 has been discussed before (Fabrika 1993).

There are two jet models in Fig. 6, in both models we have adopted our standard jet parameters,  $\dot{M}_j = 3.3 \cdot 10^{19} \text{ g/s}$  and  $2\vartheta_j = 1.5^\circ$ . There are strong discrepancies between the observed and the model spectra. Whereas the jet lines may be well fitted with one of the model (the FeXXV and FeXXVI lines of the approaching jet), the continuum divergence is dramatic. This was noticed by Brinkmann, Kotani, & Kawai (2005). They con-

<sup>1</sup> <http://heasarc.gsfc.nasa.gov/docs/xanadu/xspec/models/reflion.html>

cluded that when the line spectrum is well reproduced by the thermal jet model, but the continuum is not. We tried to use our jet model with the parameters found by Brinkmann, Kotani, & Kawai (2005), and confirmed their results. When the hard energy region of the continuum can be fitted well by adding the reflection component, the soft energy range is not.

Producing the fits shown in Fig. 6, we tried to match the spectrum best possibly to illustrate the thermal jet model limitations. The first model fits well the iron line fluxes, however we observe a strong soft deficit. The neutral hydrogen column density  $N_H$  in the fit is  $1.5 \times 10^{22} \text{ cm}^{-2}$  and the visible jet base temperature is  $\theta_0(r_0) = 17 \text{ keV}$  in the model. Note this column density is in very good agreement with the interstellar extinction in SS 433 found in optical and UV observations (Fabrika 2004). To diminish the soft deficit one must take less temperature at the jet base. The best fit we can find in this way is shown in Fig. 6 as the second model ( $N_H = 1.0 \times 10^{22} \text{ cm}^{-2}$ ,  $\theta_0(r_0) = 14 \text{ keV}$ ). It has not such a big problem in the low energy region, however the blue jet iron line fluxes can not be reproduced in this model, they are at least  $\sim 1.5$  times less than the observed fluxes. Besides that, the softest energy spectrum ( $< 1 \text{ keV}$ ) is not described well even in the second model. We conclude that the thermal jet model can not describe simultaneously the line fluxes and the soft continuum.

We have found that the thermal jet model produces about the same spectra when we keep the same value of  $\dot{M}_j^2/\Omega_j r_0 = \text{const}$ . This scaling formula is valid in the first approximation only,  $\varphi(r_0, \dot{M}_j)$  in (9) does not strongly depend on  $r_0$  and  $\dot{M}_j$  (see previous section). For instance, when we compare the thermal jet model shown in Fig. 6 by thin solid line ( $\dot{M}_j = 3.3 \cdot 10^{19} \text{ g/s}$  and  $2\vartheta_j = 1.5^\circ$ ), with another model, where we take these two parameters twice as bigger (in a limit of small angles  $\Omega_j \propto \vartheta_j^2$ ), we obtain the same model spectrum when we increase the value of  $N_H$  by 17%. Both the iron line fluxes and their equivalent widths are the same in these two models. However the line profiles appear too broad in the second case, at least during this (orbit 707) observation the jets were notably narrower than  $2\vartheta_j = 3.0^\circ$ .

It is very important to note here that (Brinkmann, Kotani, & Kawai 2005) have concluded that the thermal jet model in any combination can not produce the observed continuum. We confirm their conclusion here, and we may state the problem more concrete. When one reproduces well the continuum around the blue jet iron lines ( $\sim 6 - 10 \text{ keV}$ ), one can measure the line fluxes without strong uncertainties. One can determine then the jet visible base temperature and estimate the value of  $\dot{M}_j^2/\Omega_j r_0$  (9) using the thermal jet model. We have found in this way that the thermal jet model can not produce the lower energy continuum in SS 433. However the strongest divergence is observed in higher energy region, where about 50% of the flux is formed not in the thermal jet (Fig. 5). We have discussed above the clear evidences of the reflection in this spectral region.

We know nothing about the incident flux and its spectrum in SS 433, so we divide the whole spectrum into four parts (0.8–2.0, 2.0–4.0, 4.0–7.0 and 7.0–12.0 keV) and find the reflection model parameters independently in each part, but with the same jet parameters and the same IS absorption  $N_H$ .

The red jet spectrum has to notably contribute to the low energy region, however, it is not observed there (Kotani et al. 1996), but it is observed at higher energies (red iron lines). The lack of the red jet at low energies ( $< 4 \text{ keV}$ ) may be bound not only to its specific visibility, but with an underestimated extinction in the whole spectrum of SS 433 as well. From the XMM spectra available we can not realise clearly which effect is correct, an obscuration of a cooler portion of the red jet or an underestimated extinction in SS 433. Therefore we produce two fits, first without the red jet cooler portion in the range 0.8–4.0 keV (case A), and second with the red jet in the whole spectrum with increased  $N_H$  (case B). We find below that  $N_H$  values derived in both cases are about the same and this does not change our conclusions on the additional source of X-ray radiation in SS 433.

We estimated the column density  $N_H$  of the neutral IS absorbing material in the range 0.8–2.0 keV. In this range a strong excess of radiation is observed (Fig. 6), which does not practically depend on the thermal jet model parameters. Hereat we added a BB component, which might be an indication of the supercritical accretion disc funnel (a wind) radiation (see Section 6). In Fig. 7 we show the observed spectrum of SS 433 along with the model fits 'jet-plus-reflection' in the four spectral ranges. Table 2 presents the model parameters. The thermal jet model is identical in all ranges, yet the reflected component was fitted independently in each range (however there is no reflection in low energies).

The blue jet parameters were found in the high energy range 7.0–12.0 keV matching the model fluxes and flux ratios of the He- and H-like iron lines to the observed values. We do not see any need to use non-solar abundances of the elements, but Ni is clearly overabundant. Brinkmann, Kotani, & Kawai (2005) found the Ni abundance to be about 8 times solar. Our fits show that Ni has to be overabundant by a factor 10, since the Ni line is inside the broad absorption feature (Fig. 7d). The red jet parameters were found in the range 4.0–7.0 keV, where the red iron lines are seen clearly (Fig. 7c).

The jet parameters presented in Table 2 are more accurate than those presented in Table 1, where we used the simplest continuum model. In the precessional phase  $\psi \sim 0.0$  we find that the blue jet visible base is of  $r_{0,b} \approx 2 \cdot 10^{11} \text{ cm}$  and the gas temperature in this place is  $\theta_0 \approx 17 \text{ keV}$ . The red jet base is of  $r_{0,r} \approx 7 \cdot 10^{11} \text{ cm}$ , which is naturally explained by the obscuration of the red jet by the accretion disc (the wind) body in this orientation of the disc. In the precessional phase  $\psi \sim 0.8$ , where one may expect an obscuration of a bigger portion of the blue jet we find a lower temperature,  $\theta_0 \approx 15 \text{ keV}$ . However,  $r_{0,b}$  is about the same in both precessional phases. The spectra taken at  $\psi \sim 0.8$  are notably noisier than the one taken at  $\psi \sim 0.0$ .

Finding accurate jet parameters is not the main purpose of the present paper. The results depend on the natural variability in the jet activity, besides that the physical picture may be more complex (possible gas clumping, heating effects due to kinetic energy dissipation or the funnel radiation). However, the derived jet visible base  $r_{0,b} \sim 2 \cdot 10^{11} \text{ cm}$  is too small, while it has to be about  $10^{12} \text{ cm}$  to satisfy the observed eclipses by the donor star. The inner hotter portions of the jet are partially eclipsed (Kawai et al. 1989; Filipova et al. 2006). The jet's length is scaled (9) as



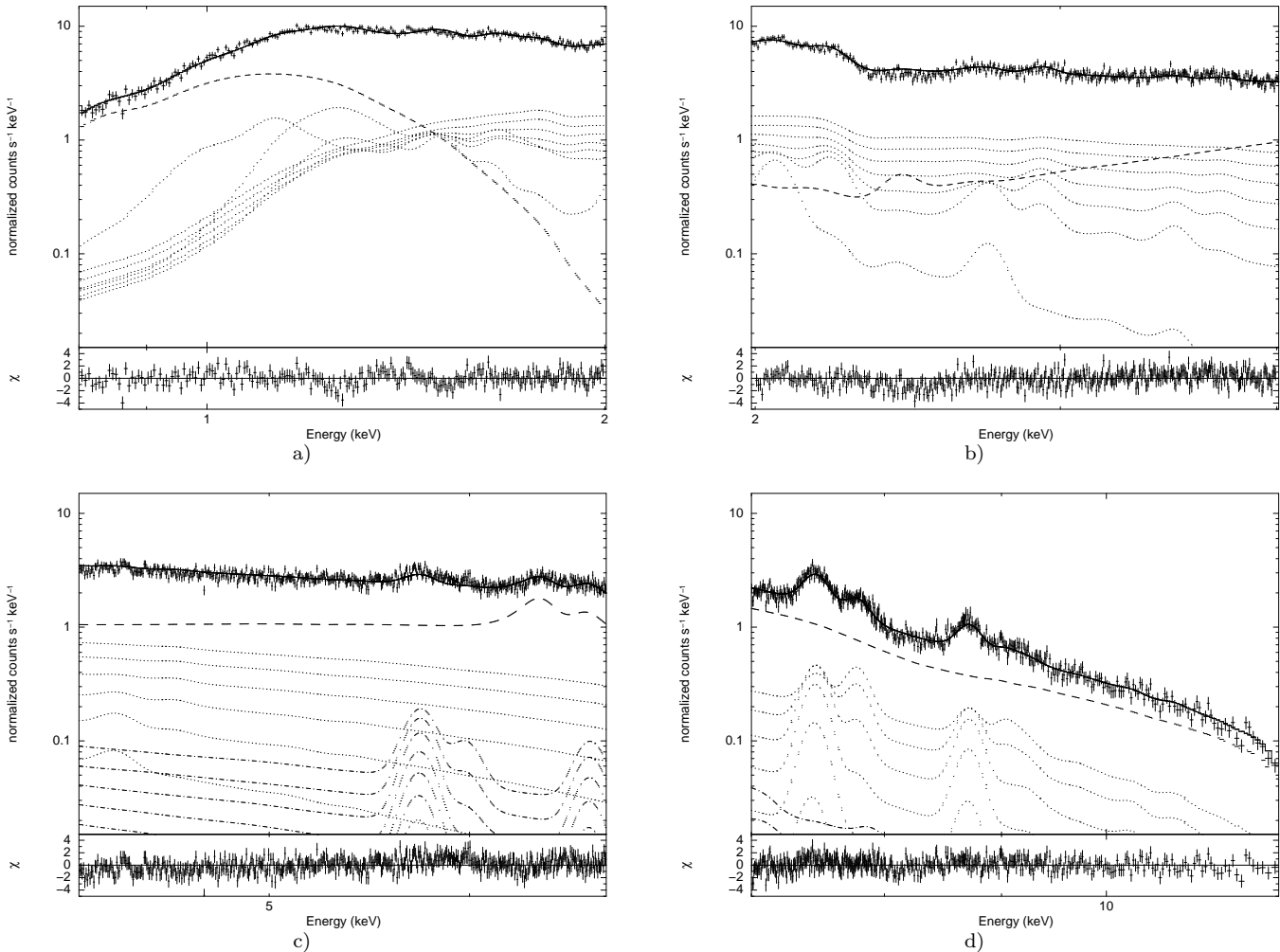


**Figure 7.** SS 433 spectra (orbit 707,  $\psi \sim 0$ ) with the model 'jets-plus-reflection' fit in four spectral ranges for case A, with zero red jet contribution in the ranges 0.8–4.0 keV (Table 2). The brightest jet components of the multi-temperature model are shown by dotted lines for the blue jet and dash-dotted lines for the red jet, the total model spectrum is shown by solid line. **a)** 0.8–2.0 keV range, where we added a black body spectrum to describe a soft excess observed at  $\sim 1$  keV (dashed line). **b)** 2.0–4.0 keV, where the reflected spectrum (dashed line) contribution weakens notably at lower energies. It is indicated by some excess in the observed spectrum at  $\sim 2.2 - 2.6$  keV. **c)** 4.0–7.0 keV, where the reflection well describes both the continuum radiation, the fluorescent line of quasi-neutral iron and the recombination Fe XXV line near 6.7 keV. Some excess at lower energies of the observed continuum is related to the change of the incident radiation spectral index (idem as in the previous range). **d)** 7–12 keV range is very well described by the reflection both in the continuum and in the broad absorption feature (Kubota et al. 2007).

$r_0 \propto \dot{M}_j^2 / \Omega_j$ , and one may scale the length to about the expected value of  $\sim 10^{12}$  cm in the thermal jet model which we use.

The reflection model produces a very good fit in the high energy range 7.0–12.0 keV ( $\chi^2 = 1.05$ ), it describes well both the whole continuum and the broad absorption feature detected by Kubota et al. (2007). The feature is located between the blue shifted Fe XXVI and Ni XXVII lines and partly covers these lines (Fig. 7d). The parameters of the reflection are found, the ionization parameter of the irradiated surface is  $\xi \approx 300$  and the illuminating radiation index is  $\Gamma \approx 2$ . This means a flat ( $EF_E$ ) spectrum of the incident radiation in this range.

In the range 4.0–7.0 keV we have an equally good agreement between the observed spectrum and the model. The reflection features at 6.2–6.8 keV are well produced.

However, in this range there is a small continuum divergence at  $\sim 4$  keV, probably due to the fact that the illuminating radiation index changes with energy. We find the index  $\Gamma \approx 1.6$  in the range, the ionization parameter is about the same as at higher energies,  $\xi \approx 240$ .

In the range 2.0–4.0 keV we observe the same effect is stronger. The model has a some deficit at 4 keV and an excess at 2 keV. An inclusion of the reflected component is essential in the range, otherwise one can not produce the observed continuum at 3–4 keV. The incident radiation has to have an index  $\Gamma < 1$  in the range. This is confirmed by a too strong emission feature at  $\approx 2.5$  keV in the reflected model. Similarly to the previous spectral range we may expect that the incident radiation index is changed with energy, and here a steeper incident spectrum is expected. The model we use

**Table 2.** Results of the spectral fits in our four spectral ranges. The upper part corresponds to the observation of orbit 707 ( $\psi \sim 0.0$ ), the bottom part, – to the orbit 609 ( $\psi \sim 0.8$ ). Case A is a model with a zero red jet contribution in softer (0.8–4.0 keV) ranges, case B with the red jet included. The jet parameters are  $\theta_0 \approx 17$  keV,  $r_{0,b} \approx 2 \cdot 10^{11}$  cm,  $r_{0,r} \approx 7 \cdot 10^{11}$  cm in the precessional phase  $\psi \sim 0.0$ , and  $\theta_0 \approx 15$  keV and the same visible jet base in  $\psi \sim 0.8$ . The lines present the ionization parameter (10) ( $\xi$ , erg/cm s), the photon index of a power law illuminating radiation  $\Gamma$ , the BB temperature in the soft X-ray range  $\theta_{bb}$  (keV), the normalisation of the BB spectrum  $\text{Norm}_{bb} = L_{39}/D_{10}^2$  ( $L_{39}$  is luminosity in units  $10^{39}$  erg/s,  $D_{10}$  is a distance in units 10 kpc), and column ISM density  $N_H$  in units  $10^{22}$  cm $^{-2}$ .  $N_H$  is equal in each range as found at lower energies.

Range, keV		7-12	4-7	2-4	0.8-2
$\xi$	A	$300 \pm 5$	$240 \pm 30$	$\approx 300$	-
	B	$300 \pm 4$	$250 \pm 30$	$\approx 300$	-
$\Gamma$	A	$2.00 \pm 0.08$	$1.56 \pm 0.05$	$\lesssim 1$	-
	B	$2.00 \pm 0.09$	$1.57 \pm 0.04$	$\gtrsim 1$	-
$\theta_{bb}$	A	-	-	-	$0.107 \pm 0.001$
	B	-	-	-	$0.100 \pm 0.001$
$\text{Norm}_{bb}$	A	-	-	-	$0.032 \pm 0.002$
	B	-	-	-	$0.125 \pm 0.005$
$N_H$	A	-	-	-	$1.54 \pm 0.01$
	B	-	-	-	$1.85 \pm 0.01$
$\chi_r^2$ (d.o.f)	A	1.05 (441)	1.28 (535)	1.39 (396)	1.39 (242)
	B	1.13 (441)	1.13 (555)	1.55 (397)	1.58 (242)
$\xi$	A	$340 \pm 80$	$300 \pm 90$	$\approx 300$	-
	B	$310 \pm 10$	$300 \pm 90$	$\approx 300$	-
$\Gamma$	A	$2.2 \pm 0.2$	$1.56 \pm 0.08$	$\lesssim 1$	-
	B	$2.0 \pm 0.2$	$1.57 \pm 0.08$	$\gtrsim 1$	-
$\theta_{bb}$	A	-	-	-	$0.093 \pm 0.004$
	B	-	-	-	$0.097 \pm 0.003$
$\text{Norm}_{bb}$	A	-	-	-	$0.026 \pm 0.003$
	B	-	-	-	$0.068 \pm 0.005$
$N_H$	A	-	-	-	$1.28 \pm 0.01$
	B	-	-	-	$1.58 \pm 0.01$
$\chi_r^2$ (d.o.f)	A	1.36 (189)	1.1 (332)	1.01 (388)	1.55 (234)
	B	1.39 (190)	1.08 (322)	1.05 (388)	1.05 (234)

is restricted by the value  $\Gamma = 1.0$ . We find then at  $\Gamma = 1.0$  the ionization parameter  $\xi \approx 300$  (with a notable scatter).

In the soft range 0.8–2.0 keV the reflected component is not detected. Even if there is a reflection in the soft range, it has other parameters than those found at higher energies. From the 7.0–12.0 keV band to the 2.0–4.0 keV band, we found a gradual decrease of the spectral index of the illuminating radiation, – from  $\Gamma \approx 2.0$  to  $\Gamma \lesssim 1$  at about the same ionization parameter,  $\xi \sim 300$ . However, an additional component related to the thermal jet one, is indeed present in the soft energy range (Fig. 6 and Fig. 7 a). Choosing the simplest way we add a BB component to describe the soft excess detected in the range.

The temperature of the BB component is  $\theta_{bb} \approx 0.11$  keV and it is identical in both our cases, A (without the red jet) and B (with the red jet). The BB component dominates at energies  $\lesssim 1$  keV and it is true again in both cases. When we do not include the red jet in the fit, the BB luminosity is  $\sim 4$  times smaller compared to the one with the red jet. However, this is rather a result of the increased  $N_H$  in the latter case (B). The soft  $\sim 1$  keV radiation is very sensitive to the  $N_H$  value, therefore we can not estimate the real luminosity in the soft excess from the XMM spectra.

In both cases we find the IS extinction value to be about the same, it is (Table 2)  $N_H \approx 1.54 \times 10^{22}$  cm $^{-2}$  in case A and  $N_H \approx 1.85 \times 10^{22}$  cm $^{-2}$  in case B. The interstellar

extinction in SS 433, found in optical and UV observations (Dolan et al. 1997), is  $A_V = 8.0 - 8.4$ . This corresponds (Predehl & Schmitt 1995) to  $N_H = (1.4 - 1.5) \times 10^{22}$  cm $^{-2}$ , which is in good agreement with the extinction found in X-rays.

Spectral residuals in the soft energy range are bigger than the ones we have in other ranges. The most prominent negative feature which is not produced in the model fit is at 1.2–1.3 keV (Fig. 7 a). However, such a feature was predicted to be present in the spectra of ULXs, if they possess a supercritical accretion disc similar to the one in SS 433, but observed nearly face-on. Fabrika, Abolmasov, & Karpov (2007) (see their Fig. 2) have simulated spectra of the multi-colour funnel model (MCF), where they introduced an Lc edge of O VIII, blueshifted to the SS 433 jet velocity. The absorption features arise inside the funnel. The model spectra being reduced with standard XSPEC models with IS absorption ( $N_H \sim 10^{22}$  cm $^{-2}$ ) produce fake broad emission/absorption features. The strongest one is an absorption feature at 1.2–1.3 keV.

Our model fits to the spectra taken at the precessional phase  $\psi \sim 0.8$  give us approximately the same results (Table 2). We find a little lower temperature and less luminosity of the soft BB component. In the sketch presented in Fig. 4 the probable reflecting region is shown at  $r > r_1$  at  $\psi \sim 0$  and  $r > r'_1$  at  $\psi \sim 0.8$  on the visible outer wall of the funnel.

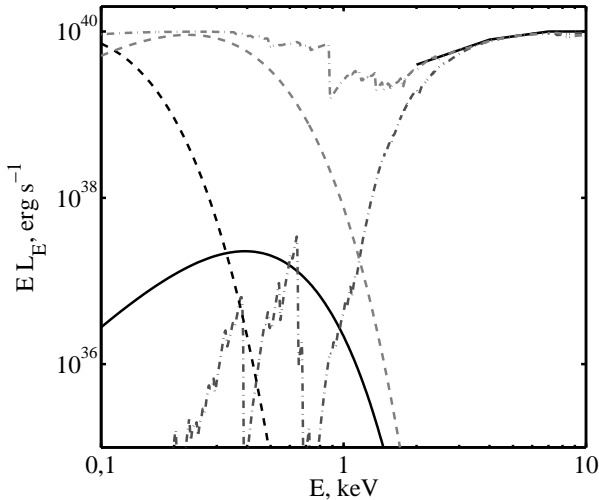


**Figure 8.** Additional components in X-ray spectrum of SS 433 (the thermal jet component is not shown). The illuminating incident radiation found in reflection model is shown by solid lines (arbitrary scaled to  $EL_E = 10^{40}$  erg/s) in three energy ranges: 2.0–4.0 keV ( $\Gamma = 1.0$ ), 4.0–7.0 keV ( $\Gamma = 1.6$ ) and 7.0–12.0 keV ( $\Gamma = 2.0$ ). The soft BB component ( $\theta_{bb} = 0.1$  keV,  $L_x \sim 3 \cdot 10^{37}$  erg/s) detected in the 0.8–2.0 keV energy range is shown by solid line. There are two originally the same flat spectra after absorption in ABSORI model with  $N_H = 10.0 \times 10^{22}$  cm $^{-2}$ ,  $\xi = 150$  (grey dash-dotted line) and  $N_H = 6.0 \times 10^{22}$  cm $^{-2}$ ,  $\xi = 3$  (bold dash-dotted line). There are two MCF (multi-colour funnel model) non-absorbed spectra with  $r_{in} = r_1 = 1.74 \cdot 10^{11}$  cm (bold dotted line) and  $r_{in} = 5 \cdot 10^{10}$  cm (grey dotted line).

If the soft excess is the visible funnel wall’s own radiation (plus a possible reflection of a soft funnel radiation), one may expect less luminosity of the wall due to the visibility conditions in the precessional phase  $\psi \sim 0.8$ .

## 6 DISCUSSION

In this section we first discuss the structure of the supercritical accretion disc wind based on the wind approach by Shakura & Syunyaev (1973), and estimate the wind and the jet funnel parameters for SS 433. Next we discuss the reflected spectrum’s origin and possible interpretations of the soft excess.

### 6.1 The expected parameters of the funnel in SS 433

The limiting Eddington luminosity is  $L_E = 4\pi GMc/\kappa = 1.5 \cdot 10^{39} m_{10}$  erg/s, corresponding limiting mass accretion rate is  $\dot{M}_E = 48\pi GM/ck = 2 \cdot 10^{19} m_{10}$  g/s, where the Thomson opacity for a gas with solar abundance is  $\kappa = 0.35$  cm $^2$ /g, and the black hole mass  $m_{10}$  is measured in 10 solar mass units. With an accretion rate at the outer disc boundary  $\dot{M}_a \gg \dot{M}_E$ , the disc becomes supercritical at spherisation radius  $r_{sp}$ . In its outer parts  $r \gtrsim r_{sp}$  the disc is subcritical,  $\dot{M}(r) = \dot{M}_a$ , below the spherisation radius  $r < r_{sp}$  the accretion regime is locally critical,  $\dot{M}(r) \sim (r/r_{sp})\dot{M}_a$  and there appears a strong wind. The total mass loss in the wind below the spherisation radius is

$\dot{M}_w(r) \sim \dot{M}_a(1 - r/r_{sp})$ . The gas is blown away by the radiation pressure and the accretion rate is decreased linearly with radius. The outflow velocity is close to that of Keplerian,  $v_w(r) \sim (GM/r)^{1/2}$ , for the bulk of the wind it is  $v_w \sim (GM/r_{sp})^{1/2}$ . Following Shakura & Syunyaev (1973), the spherisation radius is (also see Poutanen et al. (2007))

$$r_{sp} \approx \frac{3k\dot{M}_a}{8\pi c}. \quad (11)$$

This simple picture first drawn by Shakura & Syunyaev (1973) nevertheless explains the main features that we observe in SS 433 (Fabrika 2004). It is also confirmed in the main description in radiation hydrodynamic simulations (Ohsuga et al. 2005). The simple model does not account for advection effects in the disc regions close to a black hole, however, this does not change the main picture. The  $\dot{M}_w \sim \dot{M}_a$  stays the same if  $\dot{M}_a \gg \dot{M}_E$ , even the emerging spectrum of the supercritical disc does not change notably when advection is included (Poutanen et al. 2007; Takeuchi, Mineshige, & Ohsuga 2009).

Adopting the mass exchange rate in SS 433  $\dot{M}_w \sim \dot{M}_a \sim 10^{-4} M_\odot/\text{y}$  (Shklovskii 1981; van den Heuvel 1981; Fabrika 2004) we find the spherisation radius  $r_{sp} \approx 10^{10} \dot{m}_{-4}$  cm and the wind velocity  $v_w(r_{sp}) \sim 4000 (m_{10}/\dot{m}_{-4})^{1/2}$  km/s, where  $\dot{m}_{-4}$  is measured in  $10^{-4} M_\odot/\text{y}$  units. The wind velocity is directly measured in SS 433 (Fabrika 2004), it is  $\sim 100$  km/s at the polar angle  $90^\circ$  (disc edge-on) and increases sharply to  $\sim 1500$  km/s at  $60^\circ$  when the disc is the most open to observer.

Inside the spherisation radius the disc luminosity is locally Eddington, which gives the total accretion luminosity (Shakura & Syunyaev 1973) for SS 433  $L_x \sim L_E(1 + \ln \dot{M}_a/\dot{M}_E) \sim 1.0 \cdot 10^{40} m_{10}$  erg/s. Outside the funnel the radiation is thermalised ( $L_{bol} \sim L_x$ ), the wind’s photospheric radius and its temperature in the photosphere are estimated as

$$r_{ph} = \kappa \dot{M}_w / 4\pi \cos \vartheta_f v_w \sim 1 \cdot 10^{12} \text{ cm}, \quad (12)$$

$$T_{ph} = (L_{bol} / 4\pi \sigma \cos \vartheta_f r_{ph}^2)^{1/4} \sim 6 \cdot 10^4 \text{ K}.$$

Both the size of the hot body and its temperature are quite close to those we observe in SS 433. Inside the funnel where the jets are formed, the photospheric radius (the funnel bottom) is  $r_{ph,j} = \kappa \dot{M}_j / \Omega_f v_j \sim 2.5 \cdot 10^9$  cm, where  $\Omega_f = 2\pi(1 - \cos \vartheta_f)$  is the funnel’s solid angle and  $\vartheta_f = 25^\circ$ . The SS 433 jet funnel is not transparent down to the black hole. Below  $r_{ph,j}$  the funnel walls are probably not seen directly by a face-on observer.

A multicolour funnel model (MCF) has been proposed for SS 433 (Fabrika et al. 2006; Fabrika, Abolmasov, & Karpov 2007) to estimate the emerging X-ray spectrum. They considered the opaque disc wind and estimated the gas cooling and its temperature inside the wind. In the inner parts of the wind the radiation pressure dominates and  $T(r) \propto r^{-1/2}$ , in the outer parts the gas pressure dominates and  $T(r) \propto r^{-1}$ . The supercritical disc simulations (Ohsuga et al. 2005) show that the  $T(r) \propto r^{-1/2}$  is valid from  $r \sim 20 r_g$  (below which the advective energy transport is important) to  $r \sim 200 r_g \sim 10^9$  cm, approximately the outer boundary of the computational domain.

One may estimate the radiation trapping radius in the wind outflow comparing the dynamical time-scale

$t_{mov} \sim r/v(r)$  and the photon diffusion time-scale  $t_{esc} \sim n(r)r^2\sigma_T/c$ , where  $n(r) = \dot{M}_w/4\pi \cos\vartheta_f m_P r^2 v(r)$ ,  $\sigma_T$  is Thomson cross-section, and  $m_P$  is proton mass. The critical trapping radius in the wind (where  $t_{esc} = t_{mov}$ ) is  $r_{tr} \sim (2/\cos\vartheta_f)r_{sp} \sim 2r_{sp}$ . One may expect (Fabrika, Abolmasov, & Karpov 2007; Poutanen et al. 2007) that radiation is trapped within the wind up to  $r \sim 2r_{sp}$ . In this region the radiation transfer is local. In outer regions  $r \gg 2r_{sp}$  the radiation transfer inside the wind is global and radiation cools the wind ( $T(r) \propto r^{-1}$ ).

This simple approach allows us to estimate (see below) the soft excess in the spectrum observed in the low energy range (Fig. 7a). Adopting the wind temperature of  $T_{ph} \sim 60000$  K at the outer photosphere one may expect ( $T(r) \propto r^{-1}$ ) the temperature of  $T \sim 0.5$  keV at the level of spherisation radius.

Photons entering the funnel from the funnel's walls have multiple scatterings on the walls before they may finally escape the funnel. The probability to escape from the infinite funnel after one scattering is  $P = 1 - \cos\vartheta_f$ . The probability for a photon to remain in the funnel after  $N$  scatterings is  $(1 - P)^N$ . If we consider that 90% of photons escaped the funnel ( $\cos^N\vartheta_f = 0.1$ ), we find the average number of scatterings  $N(90\%) \sim 23$ , when  $\vartheta_f = 25^\circ$ . The number of scatterings in SS 433 funnel ( $r_{ph}/r_{ph,j} \sim 1000$ ) is not significantly smaller than that in the infinite funnel.

At the wall temperature of less than a few keV, as we may expect, the absorption is more probable than electron scattering. This means that the photons are re-radiated back to the funnel with the local wall temperature  $T(r)$ . The multicolour funnel has to have an integral spectrum (Fabrika et al. 2006; Fabrika, Abolmasov, & Karpov 2007) with numerous edges, where the strongest edges are from the most abundant elements like iron and oxygen. The underlying spectrum with the edges formed at about zero velocity is absolutely necessary to produce the observed stable jet outflow velocity  $v_j \approx 0.26c$  in the line-locking mechanism (Shapiro, Milgrom, & Rees 1986; Fabrika 2004).

## 6.2 The reflected and black body component

Both the reflected component which we detect in three energy ranges (Fig. 7, Table 2), and the BB component in the soft energy range 0.8–2.0 keV, may be formed at the outer visible part of the wall shown in Fig. 4 at  $r \gtrsim r_1$ . At the precessional phase  $\psi \approx 0$  we find  $r_1 \approx 0.87 r_0 \approx 1.74 \cdot 10^{11}$  cm (Table 2). The ionization parameter (10) found at the reflecting surface is  $\xi \sim 300$  and it is approximately the same in all the three energy ranges. As we discussed above, the multiple scattering in the funnel is expected, so we may consider this value of  $\xi$  as effective or averaged over all putative scatterings in the funnel. A study of the additional spectral components is out of the scope of this paper, we only make rough geometrical estimates here.

We estimate an angle  $\beta$  at which the reflecting medium is exposed to the incident radiation to produce the derived ionization parameter (10),  $\beta \sim \xi n r^2 / L_x$ . Using  $n(r)r^2 = \dot{M}_w/4\pi \cos\vartheta_f m_P v_w$ , we find  $\beta \sim \xi \dot{M}_w/4\pi \cos\vartheta_f m_P v_w L_x \sim 0.04 \dot{m}_{-4} v_{2000}^{-1} L_{40}^{-1}$  for  $\xi = 300$ , where the wind velocity is measured in units of 2000 km/s and the funnel luminosity in  $10^{40}$  erg/s units. This corresponds to the funnel depth  $\beta r_1 \sim 7 \cdot 10^9$  cm, which is close to the spherisation radius.

The reflected component luminosity found in the energy range of 7–12 keV is  $L_{refl} \sim 3.3 \cdot 10^{35} k$  erg/s (at a distance of 5.5 kpc), where the  $k$  factor is ratio of the total cone surface at  $r > r_1$  (Fig. 4) to the visible cone surface. At the precessional phase  $\psi \approx 0$ , the ratio is  $k \approx 3.2$ , and the luminosity at  $r > r_1$  is  $L_{refl} \sim 1.0 \cdot 10^{36}$  erg/s. In the range of 7–12 keV the reflection albedo is mainly geometrical and we might expect the angle  $\beta \sim F_{refl}/F_{inc}$ , where  $F_{inc}$  is the incident flux in this energy range, if the reflecting surface is directly exposed to the hard radiation from its origin. Assuming that the illuminating spectrum is flat, with total luminosity of  $\sim 10^{40}$  erg/s in the spectral range of 0.1–20 keV, we find that its luminosity in the 7–12 keV range is  $F_{inc} \sim 10^{39}$  erg/s and the angle  $\beta \sim F_{refl}/F_{inc} \sim 0.001$ . This gives us an estimate of the funnel depth, where the illuminating radiation is formed,  $\beta r_1 \sim 2 \cdot 10^8$  cm.

The funnel photosphere radius,  $r_{ph,j} \sim 2.5 \cdot 10^9$  cm, derived from the observed values ( $\dot{M}_j, v_j$ ), is notably greater than the last estimate of the radius where the hard illuminating radiation is formed. Indeed, the reflecting surface may not directly see the deepest funnel parts. There have to be multiple scatterings in the funnel where the harder ( $> 7$  keV) radiation may survive absorption.

In Fig. 8 we show the illuminating spectrum found above in the 4–12 keV energy range, arbitrarily scaled to the luminosity of  $10^{40}$  erg/s. We show the spectral slope in the 2–4 keV range  $\Gamma = 1.0$ , but it was noted above that it has to be steeper,  $\Gamma < 1$ . The figure also shows two originally flat absorbed spectra. These two absorbed spectra illustrate two limiting cases between which one may expect to find true picture. Even very thick ( $N_H \sim 10^{23}$  cm $^{-2}$ ) medium of higher ionization ( $\xi = 150$ ) can not depress the radiation spectrum below 3–4 keV. Lower ionization medium ( $\xi = 3$ ) does absorb the radiation effectively.

Therefore we expect an existence of an absorbing (reflecting) medium inside the funnel, which produces such a curved spectrum of radiation, illuminating the reflected surface. Note that having He- and H-like absorption edges at about zero velocity is a mandatory property of the funnel spectrum to produce the observed stable jet velocity ( $v_j \approx 0.26c$ ) due to the line-locking mechanism (Shapiro, Milgrom, & Rees 1986; Fabrika 2004).

Inspecting the results of the supercritical accretion disc simulations by Ohsuga et al. (2005) we find that the walls at the level of  $\sim 10^8 - 10^9$  cm consist of a low velocity gas with the temperature of  $T \sim 2 \cdot 10^6$  K and the density of  $n \sim (1 - 3) \cdot 10^{18}$  cm $^{-3}$ . The walls are the source of strong wind, they supply the funnel with the gas. The funnel walls' photosphere with the temperature from  $T \sim 10^7$  K at  $r \sim 10^8$  cm to  $T \sim 10^6$  K at  $r \sim 10^9$  cm, may be the source of the edged radiation spectrum.

The nearly flat spectrum of the funnel (Fig. 7, 8), which is expected to illuminate the reflecting surface, extends at least from 4 to 12 keV. The supercritical accretion disc spectrum is expected to be flat (Poutanen et al. 2007), however, it is supposed to go up to a few keV only. The Comptonization may extend and flatten the spectrum to higher energies. At an accretion rate of  $\sim 10\%$  of the Eddington rate, the local emitted spectrum in the inner region of the disc is approximated by a diluted BB with the spectral hardening factor  $f \sim 1.7$  (Shimura & Takahara 1995). For the accretion rates close to the Eddington limit,  $f$  increases and may

amount to 10. This may extend the disc spectrum to higher energies.

Inside the disc spherisation radius, the disc wind supplies the funnel with gas starting from very deep regions (Shakura & Syunyaev 1973; Eggum, Coroniti, & Katz 1988; Okuda et al. 2005; Ohsuga et al. 2005), this gas is directly accelerated by the funnel radiation. The interaction of the gas accelerated to the velocities of  $\sim 0.2 - 0.3c$  with new portions of the walls' wind creates the conditions quite suitable for Comptonization. These conditions might be about the same throughout the whole funnel length where the jet is formed, as the high-speed outflow has about the same velocity.

In the INTEGRAL observations a hard X-ray emission (20 – 100 keV) with the total hard luminosity of  $\sim 10^{35}$  erg/s has been detected (Cherepashchuk et al. 2005), which may be well explained (Krivosheyev et al. 2009) in terms of Comptonized thermal plasma surrounding the visible jet base.

Despite the fact that the jet formation and collimation mechanism is not clear yet, one may expect the Comptonization is significant inside the funnel. The observed spectrum, taken when the disc is the most open to the observer (Krivosheyev et al. 2009), is nearly flat in the energy range of 10–20 keV. This spectrum may be a continuation of the flat 7–12 keV spectrum found here in the reflecting model.

The soft excess detected in the SS 433 spectra and introduced here as a BB component with the temperature of  $\theta_{bb} \approx 0.1$  keV (Table 2, Fig. 8), may appear to be the direct radiation of the visible funnel wall at  $r > r_1$  (Fig. 4). When we take into account the factor  $k \approx 3.2$ , which is a ratio of the total cone surface at  $r > r_1$  to the visible cone surface, we find the soft BB component luminosity  $L_x \sim 3 \cdot 10^{37}$  erg/s.

The soft BB component is shown in Fig. 8. Note that the luminosity of the soft component strongly depends on the adopted column density  $N_H$ . It is essential here that the soft component is necessary (Brinkmann, Kotani, & Kawai 2005, and herein) in order to understand the SS 433 spectra within the framework of the thermal jet model.

In Fig. 8 we show two versions of the funnel's non-absorbed spectrum in the MCF model (Fabrika et al. 2006; Fabrika, Abolmasov, & Karpov 2007), at  $r > 1.74 \cdot 10^{11}$  cm (the value of  $r_1$  derived above) and  $r > 5 \cdot 10^{10}$  cm. Deriving these spectra, we adopted the wind's photosphere radius and the temperature of  $r_{ph} = 10^{12}$  cm,  $T_{ph} = 50000$  K respectively (12), and  $T(r) \propto r^{-1}$  as it was discussed above. This illustrates that the MCF spectra might be responsible for the soft excess observed in SS 433. Nevertheless, one can say nothing else, except that the additional soft component is present in SS 433 spectrum.

The soft excess is observed in the spectra of ULXs (Stobbart, Roberts, & Wilms 2006; Roberts 2007; Poutanen et al. 2007), their temperature is  $\theta \sim 0.1$  keV and it contributes to the total ULX luminosity of  $\sim 10\%$ . The soft component luminosity in ULXs is about  $10^{38} - 10^{39}$  erg/s. If the ULXs are nearly face-on SS 433 stars, their intrinsic soft component luminosity has to be some less because of the geometrical beaming of their supercritical discs. However, the soft X-ray luminosity is model dependent, it strongly depends on the adopted absorption value.

## 7 CONCLUSION

The goal of the present paper was to find indications of the supercritical accretion disc funnel in SS 433 X-ray radiation. The bolometric luminosity of the disc in SS 433 is  $\sim 10^{40}$  erg/s and all the luminosity must be initially released in X-rays. This is confirmed by the well-established kinetic luminosity of SS 433 jets, which is  $\sim 10^{39}$  erg/s, and the fact that the jets are formed in the deepest places of the disc funnel close to the black hole. The observed X-ray luminosity of SS 433 is  $\sim 10^{36}$  erg/s and it is the radiation of the cooling X-ray jets. Both the orientation of SS 433 and the visibility conditions do not allow us to see any deep areas of the funnel. However, the strong mass loss of the accretion disc gives us a hope for detecting some indications of the funnel radiation.

We have analysed the XMM spectra of SS 433 with a well-known standard model of the adiabatically cooling X-ray jets, taking into account cooling by radiation. We confirm that the thermal jet model reproduces the emission line fluxes quite well. When the disc is most open to the observer, the visible blue jet base is  $r_0 \approx 2 \cdot 10^{11}$  cm, the gas temperature at  $r_0$  is  $\theta_0 \approx 17$  keV. The IS gas column density is  $N_H \sim 1.5 \cdot 10^{22}$  cm $^{-2}$ , which is in good agreement with the IS extinction found in optical and UV observations. We confirm the previous finding (Kotani et al. 1996; Brinkmann, Kotani, & Kawai 2005) that the red jet is probably not seen (blocked) in the soft energy range of 0.8–2.0 keV. However, both the model with blocked the red jet portions, and the model with the whole red jet visible (but with some higher  $N_H$ ) give the same result, that the thermal jet model alone can not explain the soft continuum. We also confirm that Nickel is highly overabundant in the jets (Kotani et al. 1996; Brinkmann, Kotani, & Kawai 2005).

We have adopted the luminosity  $L_k = 10^{39}$  erg/s and the jet opening angle  $2\vartheta_j = 1.5^\circ$  as well established and known. However, the derived jet visible base  $r_0$  is too small, it has to be  $\sim 10^{12}$  cm to satisfy the observed eclipses by the donor star. Using the scaling formula  $r_0 \propto \dot{M}_j^2 / \Omega_j$  one may find that during these XMM observations the jet kinetic luminosity was  $L_k \sim 2 \cdot 10^{39}$  erg/s. This scaling should not change the thermal jet spectrum.

We find that the thermal jet model alone can not reproduce the continuum radiation in the XMM spectral range. Therefore we use the thermal jet model together with the REFLION ionized reflection model and find quite a good representation of the spectra. Introducing the reflection not only explains the continuum curvature at the energies of  $> 3 - 4$  keV and the fluorescent line of quasi-neutral iron, it reproduces the broad absorption feature at  $\sim 8$  keV recently detected by Kubota et al. (2007). We independently study three energy ranges (2–4, 4–7 and 7–12 keV) with the same thermal jet model to find the reflection parameters. We find that the ionization parameter (10) is about the same in these ranges,  $\xi \sim 300$ , which indicates a highly ionized reflection surface. The illuminating radiation photon index changes from flat,  $\Gamma \approx 2$ , in the 7–12 keV range to  $\Gamma \approx 1.6$  in the range 4–7 keV and to  $\Gamma \lesssim 1$  in the range 2–4 keV.

We conclude that the additional reflected spectrum is an indication of the funnel radiation. The illuminating radia-

tion spectrum is flat in the range of 7–12 keV. With multiple scatterings in the funnel the hard radiation may survive absorption. The reflected luminosity in this 7–12 keV spectral range is  $L_{refl} \sim 10^{36}$  erg/s. The softer (2–7 keV) part of the illuminating spectrum (Fig. 8) carries a trace of absorption. This is assumed to be due to the multiple scatterings in the funnel. It is important to note that an existence of He- and H-like absorption edges at about zero velocity is a mandatory property of the funnel spectrum to be able to produce the observed jet velocity due to the line-locking mechanism.

The supercritical accretion disc spectrum is expected to be flat, however, it extends up to a few keV only. Comptonization may extend and flatten the spectrum to higher energies. The interaction of the high velocity gas moving along the jet axis with the walls' wind makes the conditions for the Comptonization throughout the whole funnel length consistent. Direct evidences of the Comptonized radiation have recently been found in the INTEGRAL observations (Cherepashchuk et al. 2005).

We have not found any evidences of the reflection in the soft 0.8–2.0 keV energy range. The soft excess is detected in the SS 433 spectra. We suppose that in the soft X-rays we observe direct radiation of the visible funnel wall. We represented this component as a black body radiation with a temperature of  $\theta_{bb} \approx 0.1$  keV and luminosity of  $L_{BB} \sim 3 \cdot 10^{37}$  erg/s. The soft excess may be also fitted with a multicolour funnel (MCF) model. Both the soft X-ray luminosity and its derived spectrum strongly depend on the column density  $N_H$ . The soft component is necessary to add in order to understand the SS 433 spectra within the framework of the thermal jet model.

The soft excess is observed in the spectra of ULXs with the soft component temperature of  $\theta \sim 0.1$  keV, which is identical with that found in SS 433. If the ULXs or some of them are nearly face-on versions of SS 433, one may adjust their soft X-ray components to the outer funnel walls radiation (Poutanen et al. 2007).

## 8 ACKNOWLEDGEMENTS

The authors thank Victor Doroshenko for useful comments and discussions, and Anna Zyazeva for the correction of this manuscript. The research was supported by RFBR grant 07-02-00909.

## REFERENCES

- Berghea C. T., Weaver K. A., Colbert E. J. M., Roberts T. P., 2008, *ApJ*, 687, 471  
 Blundell K. M., Bowler M. G., 2004, *ApJ*, 616, L159  
 Blundell K. M., Bowler M. G., Schmidtbreick L., 2008, *ApJ*, 678, L47  
 Borisov N. V., Fabrika S. N., 1987, *SvAL*, 13, 200  
 Brinkmann W., Fink H. H., Massaglia S., Bodo G., Ferrari A., 1988, *A&A*, 196, 313  
 Brinkmann W., Kawai N., Matsuoka M., Fink H. H., 1991, *A&A*, 241, 112  
 Brinkmann W., Kotani T., Kawai N., 2005, *A&A*, 431, 575  
 Cherepashchuk A. M., Aslanov A. A., Kornilov V. G., 1982, *AZh*, 59, 115  
 Cherepashchuk A. M., et al., 2005, *A&A*, 437, 561  
 Dolan J. F., et al., 1997, *A&A*, 327, 648  
 Dubner G. M., Holdaway M., Goss W. M., Mirabel I. F., 1998, *AJ*, 116, 1842  
 Eggum G. E., Coroniti F. V., Katz J. I., 1988, *ApJ*, 330, 142  
 Eikenberry S. S., Cameron P. B., Fierce B. W., Kull D. M., Dror D. H., Houck J. R., Margon B., 2001, *ApJ*, 561, 1027  
 Fabrika S. N., 1993, *MNRAS*, 261, 241  
 Fabrika S., 2004, *ASPRv*, 12, 1  
 Fabrika S. N., Borisov N. V., 1987, *SvAL*, 13, 279  
 Fabrika S., & Mescheryakov, A. 2000, *JENAM* (Joint European and National Astronomical Meeting) , 74  
 Fabrika S., Mescheryakov A., 2001, *IAUS*, 205, 268  
 Fabrika S., Karpov S., Abolmasov P., Sholukhova O., 2006, *IAUS*, 230, 278  
 Fabrika S. N., Abolmasov P. K., Karpov S., 2007, *IAUS*, 238, 225  
 Filippova E., Revnivtsev M., Fabrika S., Postnov K., Seifina E., 2006, *A&A*, 460, 125  
 Gies D. R., Huang W., McSwain M. V., 2002, *ApJ*, 578, L67  
 Goranskii V. P., Esipov V. F., Cherepashchuk A. M., 1998, *ARep*, 42, 209  
 Hillwig T. C., Gies D. R., 2008, *ApJ*, 676, L37  
 Katz J. I., 1987, *ApJ*, 317, 264  
 Kawai N., Matsuoka M., Pan H.-C., Stewart G. C., 1989, *PASJ*, 41, 491  
 Kotani T., Kawai N., Matsuoka M., Brinkmann W., 1996, *PASJ*, 48, 619  
 Krivosheyev Y. M., Bisnovatyi-Kogan G. S., Cherepashchuk A. M., Postnov K. A., 2009, *MNRAS*, 394, 1674  
 Kubota K., Kawai N., Kotani T., Ueda Y., Brinkmann W., 2007, *ASPC*, 362, 121  
 Lopez L. A., Marshall H. L., Canizares C. R., Schulz N. S., Kane J. F., 2006, *ApJ*, 650, 338  
 Marshall H. L., Canizares C. R., Schulz N. S., 2002, *ApJ*, 564, 941  
 Murdin P., Clark D. H., Martin P. G., 1980, *MNRAS*, 193, 135  
 Namiki M., Kawai N., Kotani T., Makishima K., 2003, *PASJ*, 55, 281  
 Ohsuga K., Mori M., Nakamoto T., Mineshige S., 2005, *ApJ*, 628, 368  
 Okuda T., Teresi V., Toscano E., Molteni D., 2005, *MNRAS*, 357, 295  
 Panferov A. A., Fabrika S. N., 1997, *ARep*, 41, 506  
 Poutanen J., Lipunova G., Fabrika S., Butkevich A. G., Abolmasov P., 2007, *MNRAS*, 377, 1187  
 Predehl P., Schmitt J. H. M. M., 1995, *A&A*, 293, 889  
 Roberts, T.P. 2007, *Ap&SS*, 311, 203  
 Ross R. R., Fabian A. C., Young A. J., 1999, *MNRAS*, 306, 461  
 Ross R. R., Fabian A. C., 2005, *MNRAS*, 358, 211  
 Shakura N. I., Syunyaev R. A., 1973, *A&A*, 24, 337  
 Shapiro P. R., Milgrom M., Rees M. J., 1986, *ApJS*, 60, 393  
 Shimura T., Takahara F., 1995, *ApJ*, 445, 780  
 Shklovskii I. S., 1981, *SvA*, 25, 315  
 Smith R. K., Brickhouse N. S., 2000, *RMxAC*, 9, 134  
 Smith R. K., Brickhouse N. S., Liedahl D. A., Raymond

- J. C., 2001a, ApJ, 556, L91  
Smith R. K., Brickhouse N. S., Liedahl D. A., Raymond  
J. C., 2001b, ASPC, 247, 161  
Stobart A.-M., Roberts T. P., Wilms J., 2006, MNRAS,  
368, 397  
Takeuchi S., Mineshige S., Ohsuga K., 2009, arXiv,  
arXiv:0904.4598  
van den Heuvel E. P. J., 1981, VA, 25, 95  
Zealey W. J., Dopita M. A., Malin D. F., 1980, MNRAS,  
192, 731